Received: 24 July 2025 | Revised: 24 September 2025 | Accepted: 3 October 2025

DOI: 10.1002/inf2.70095

RESEARCH ARTICLE

WILEY

Delicate design of lithium-ion bridges in hybrid solid electrolyte for wide-temperature adaptive solid-state lithium metal batteries

Yuchen Wang[1,2,3] | **Kun Liu**[4] | **Henghui Xiao**[1] | **Zhaorun Zhu**[1] | **Chenqun Hong**[1] | **Hongzhen Lin**[3] | **Jian Wang**[5,6] | **Decai Guo**[4] | **Meinan Liu**[1]

[1]Guangxi Key Laboratory of Processing for Non-Ferrous Metals and Featured Materials, MOE Key Laboratory of New Processing Technology for Non-Ferrous Metals and Materials, Guangxi Key Laboratory of Electrochemical Energy Materials, School of Resources, Environment and Materials, Guangxi University, Nanning, the People's Republic of China

[2]State Key Laboratory of Fine Chemicals, Frontiers Science Center for Smart Materials, PSU-DUT Joint Center for Energy Research, School of Chemical Engineering, Dalian University of Technology, Dalian, the People's Republic of China

[3]i-Lab, Suzhou Institute of Nano-Tech and Nano-Bionics, Chinese Academy of Sciences, Suzhou, the People's Republic of China

[4]Section 14, Dalian Research Institute of Petroleum and Petrochemicals, SINOPEC, Dalian, the People's Republic of China

[5]Helmholtz Institute Ulm (HIU), Ulm, Germany

[6]Karlsruhe Institute of Technology (KIT), Karlsruhe, Germany

Correspondence
Jian Wang, Karlsruhe Institute of Technology (KIT), Karlsruhe D76021, Germany.
Email: jian.wang@kit.edu; wangjian2014@sinano.ac.cn

Decai Guo, Section 14, Dalian Research Institute of Petroleum and Petrochemicals, SINOPEC, Dalian 116045, the People's Republic of China.
Email: guodecai.fshy@sinopec.com

Meinan Liu, Guangxi Key Laboratory of Processing for Non-Ferrous Metals and Featured Materials, MOE Key Laboratory of New Processing Technology for Non-Ferrous Metals and Materials, Guangxi Key Laboratory of Electrochemical Energy Materials, School of Resources, Environment and Materials, Guangxi University, Nanning 530004, the People's Republic of China.
Email: meinanliu@gxu.edu.cn

Funding information
Open Project of State Key Laboratory of Inorganic Synthesis and Preparative Chemistry, Grant/Award Number: 2025-8; Alexander von Humboldt Foundation;

Abstract

Hybrid solid electrolytes have emerged as promising candidates for next-generation high-energy-density solid-state lithium metal batteries owing to the enhanced safety and processability. Nevertheless, the practical implementation remains hindered by severe interfacial Li^+ transport barriers at ceramic-polymer junctions, particularly under ambient low-temperature or high-power-density surroundings. Herein, the lithium-ion bridge concept has been proposed to accelerate Li^+ transport kinetics across the ceramic-polymer interphase through the delicate design of a chemical bonding strategy. As demonstrated, the poly(vinylidene fluoride-co-hexafluoropropylene) (PH) chain with $Li_{6.4}La_3Zr_{1.4}Ta_{0.6}O_{12}$ (LLZTO) particles can be connected by lithium benzene sulfonate as Li^+ conductive bridges. With these Li^+ bridges, this unique hybrid PH-LLZTO solid-state electrolyte exhibits an exceptional ionic conductivity of 0.71 mS cm^{-1} at 25°C with a superior Li^+ transference number of 0.67. Impressively, this advanced solid-state electrolyte empowers high-voltage $LiNi_{0.8}Co_{0.1}Mn_{0.1}O_2$/Li cells under fast charge/discharge capability as high as 4C and a wide temperature range from −20°C to 60°C. Consequently, the optimal solid-state Li metal battery could stabilize at −20°C with a high discharge specific capacity of 130 mAh g^{-1}. Moreover, a bipolar pouch cell by stacking 4 units can be successfully assembled using this advanced solid-state electrolyte

Special Fund for Science and Technology Development of Guangxi, Grant/Award Number: AD25069078; National Natural Science Foundation of China, Grant/Award Numbers: 22075313, 22379160; Key Laboratory of Engineering Dielectrics and Its Application (Harbin University of Science and Technology), Grant/Award Number: KFM202507

with fast Li^+ transport kinetics and delivers an ultra-high voltage of 15.12 V, showcasing the great potential of integrated module application in the future.

KEYWORDS

high ion conduction, high power density, hybrid solid electrolyte, lithium metal battery, lithium-ion bridges, temperature adaption

1 | INTRODUCTION

As informatization progresses in modern society, driven by escalating demands for electric vehicles and portable electronics, the relentless pursuit of higher energy-density storage systems has catalyzed global research initiatives to engineer next-generation battery systems with optimized electrode/electrolyte materials.[1–4] Among all the candidates, lithium metal batteries (LMBs) emerge as the foremost candidate to supersede conventional lithium-ion technologies, capitalizing on the high theoretical capacity (3860 mAh g^{-1}) and low potential.[5–8] Nevertheless, the inherent flammability and volatile leakage risks of conventional organic liquid electrolytes critically compromise the operational safety of LMBs.[9,10] To overcome these critical limitations, substantial research efforts are being directed toward developing stable solid-state electrolyte systems as safer alternatives to liquid electrolytes.[11]

Solid-state electrolytes (SSEs), especially polymer and ceramic-based electrolytes, have garnered significant attention for their intrinsic non-flammability.[12–14] Among them, solid polymer electrolytes (SPEs) exhibit excellent interfacial compliance with electrodes but suffer from ionic conductivities orders of magnitude below those of liquid electrolytes, often requiring elevated temperatures to achieve acceptable performance.[15,16] Alternatively, ceramic SSEs (e.g., $Li_7La_3Zr_2O_{12}$ [LLZO], $Li_{3x}La_{2/3-x}TiO_3$ [LLTO], and $Li_{1+x}Al_xTi_{2-x}(PO_4)_3$ [LATP]) demonstrate superior room-temperature conductivity (10^{-4}–10^{-3} S cm^{-1}) and dendrite-blocking mechanical strength (>10 GPa).[17–19] Yet, their rigid ceramic-electrode interfaces induce catastrophic interfacial impedance, causing severe polarization and rapid capacity fade under practical current densities.[20] To mitigate such interfacial issues, various interfacial engineering strategies have been explored, such as applying artificial interlayers (e.g., AlF_3, Li_3P)[21,22] to mitigate parasitic reactions and surface modifications to enhance lithium affinity.[23,24] Despite the progress achieved in alleviating interfacial issues, these approaches are often accompanied by inevitable trade-offs, in which lowering interfacial resistance comes at the expense of ionic conductivity, whereas enhancing conductivity frequently introduces new interfacial instabilities, thereby making it challenging to simultaneously realize high ionic conductivity and low interfacial resistance.

Against this backdrop, hybrid solid electrolytes (HSEs) which combine polymer with ceramic components have emerged as promising candidates for safer, high-energy batteries. Currently, the state-of-the-art technology for preparing high-performance HSEs is by compounding Li-conducting fillers such as $Li_{6.75}La_3Zr_{1.75}Ta_{0.25}O_{12}$[25] and $Li_{1.4}Al_{0.4}Ti_{1.6}(PO_4)_3$,[26] thereby combining the flexible processability of polymers with the high ionic conductivity of ceramics. However, a critical bottleneck in HSEs is the presence of numerous interfaces, including those filler particles as well as the interface between filler and the polymer matrix, which severely restricts Li^+ conduction, and it remains challenging to achieve continuous Li^+ transport across these interfacial regions.[27,28] To overcome this intrinsic limitation, the most straightforward strategy is to increase the ceramic filler content. With the incorporation of fillers, Li-rich space-charge layers are established on the ceramic filler surface.[29] Once the loading surpasses the percolation threshold, these interfacial regions progressively interconnect to construct a continuous percolating network, enabling rapid Li^+ migration along the interfaces and thereby substantially enhancing ionic conductivity.[30] Nevertheless, such percolation channels inherently rely on filler-induced space-charge layers, which leads to limited transport efficiency and compromised stability. Moreover, achieving percolation typically requires extremely high ceramic loading and is highly sensitive to particle size, shape, and dispersion, together with limited universality across different systems.

Alternatively, in contrast to conventional ceramic fillers, several functional composite fillers, including $BaTiO_3$-$Li_{0.33}La_{0.56}TiO_{3-x}$ nanowires,[31] [EMIM][TFSI]-coated $Li_3Zr_2Si_2PO_{12}$ (LZSP)[32] and single-ion lignin-based lithium salt (L-Li)[33] have been developed to improve filler dispersion and interfacial compatibility, partially mitigating the impedance-conductivity trade-off. Nevertheless, similar to percolating channels, the conduction pathways in these systems still rely primarily on dynamic charge transfer processes and the generated built-in

electric field, which cannot fundamentally resolve the interfacial transport issue. Accordingly, the pursuit of innovative interfacial design strategies that can architect stable and continuous Li^+ transport networks is essential to surmounting the long-standing interfacial bottleneck and charting a viable pathway toward the practical realization of HSEs.

Herein, a straightforward and effective interfacial engineering strategy is proposed to address this polymer-ceramic interphase concerns in HSEs. Through precise interfacial engineering, $Li_{6.4}La_3Zr_{1.4}Ta_{0.6}O_{12}$ (LLZTO) is uniformly grafted onto poly(vinylidene fluoride-co-hexafluoropropylene) (PVDF-HFP) chains (PH-LLZTO) via chemical binding linkage (Figure 1A). Such chemical binding constructs robust Li^+ bridges that not only minimize interfacial resistance but also establish continuous and efficient Li^+ conduction pathways across the polymer-ceramic phases. This design represents a paradigm shift from a physical mixture to a chemically integrated ionic network. With these robust Li^+ bridges, the PH-LLZTO-based cells demonstrate exceptional interfacial stability with both lithium metal anodes and high-voltage cathodes. Li|PH-LLZTO|Li symmetric cells achieve unprecedented cycling stability exceeding 1000 h at 0.2 mA cm^{-2}, while maintaining stable operation for 800 h even under elevated current density of 0.5 mA cm^{-2}. Furthermore, the high-voltage solid-state $LiNi_{0.8}Co_{0.1}Mn_{0.1}O_2$ (NCM811)|PH-LLZTO|Li batteries deliver exceptional operational performance at high current density of 4 C and wide temperature operation (−20°C to 60°C). Impressively, even at such a low temperature −20°C, the solid-state batteries preserve 100% capacity retention over 60 cycles with a stable discharge capacity of 130 mAh g^{-1}. The excellent comprehensive performance of HSE charts a technologically viable roadmap toward high-energy-density SSEs with industrial-grade reliability.

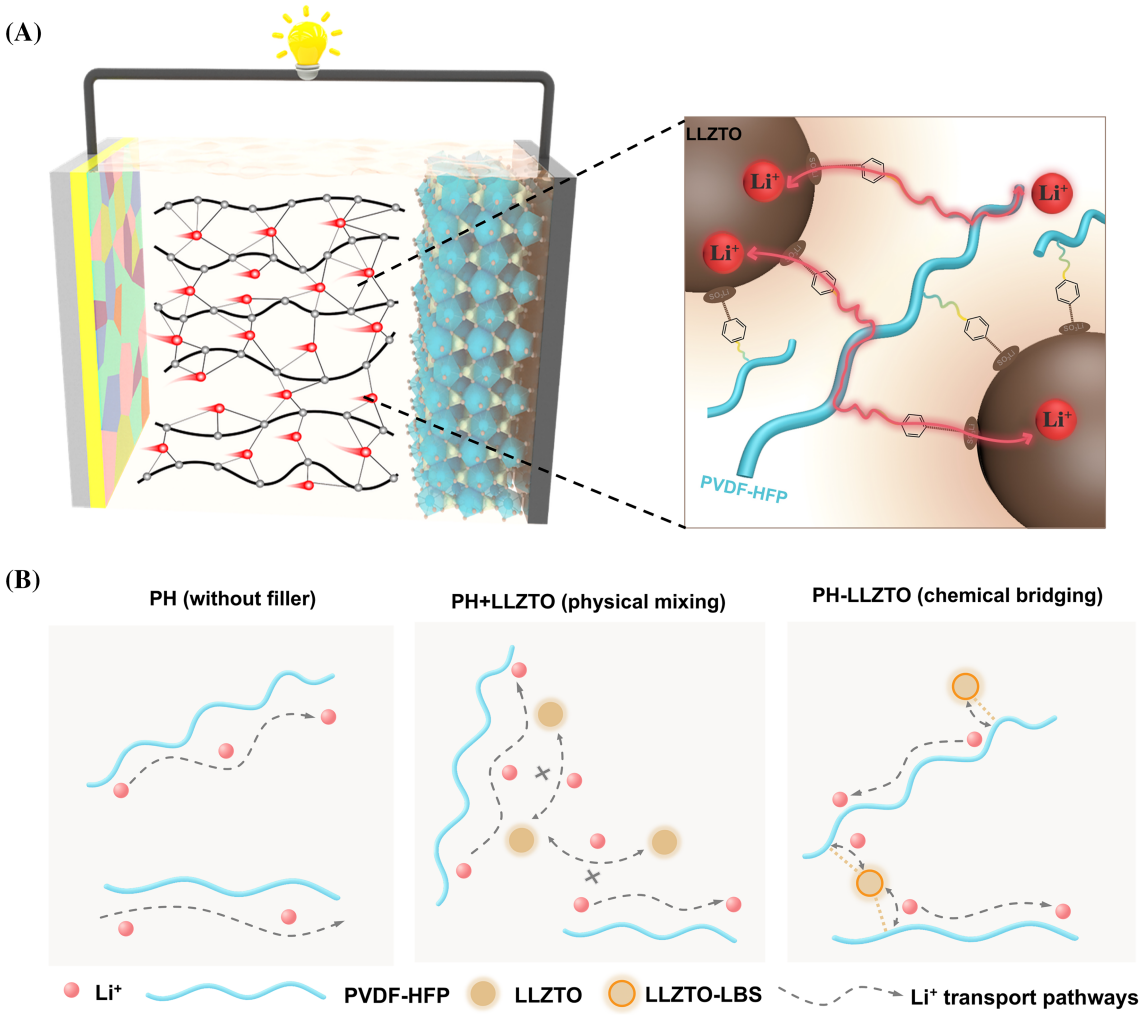

FIGURE 1 (A) Schematic illustrations of Li^+ transport pathway of PH-LLZTO electrolyte. (B) Different Li^+ conduction modes in PH, PH + LLZTO, and PH-LLZTO electrolytes.

2 | RESULTS AND DISCUSSIONS

The fabrication of PH-LLZTO is schematically illustrated in Figure S1, and the most critical step is the alkylation reaction between phenyl and olefin groups.[34] Firstly, benzene sulfonic acid (BS) reacts with lithium hydroxide (LiOH) to form lithium benzenesulfonate (LBS) (Figure S1A), as evidenced by x-ray photoelectron spectroscopy (XPS) analysis (Figure S5A). It can be observed that S 2p peaks at 170.1 eV and 168.8 eV in BS assigned to the -SO_3H anchoring group on aromatic rings remain well in LBS.[35] While the emergence of a distinct Li 1s peak at 55.3 eV in LBS and the shifted O 1s peak in LBS compared to BS well verify that the H atom is indeed replaced by the Li atom. Due to the strong interaction between lithium sulfonate groups (-SO_3Li) in LBS and the surface-exposed metal (La, Zr, Ta, Li) on LLZTO,[36] LBS can be tightly anchored onto the surface of LLZTO (Figure S1B). Subsequently, the alkaline environment created by LiOH solution facilitates the dehydrofluorination of PVDF-HFP, leading to the formation of C═C double bonds in the resulting structure (PH-HF), as demonstrated in Figure S1C.[37] Finally, the surface-exposed phenyl group on LBS can react with alkali-derived C═C dienes within dehydrofluorinated PVDF-HFP, achieving LLZTO uniformly grafted on PVDF-HFP (PH-LLZTO), as shown in Figure S1D.[34] To circumvent the potential reaction between FSI^- and the C═C bond,[38] lithium bisfluorosulfonimide (LiFSI) was strategically introduced after all processes were completed. For a well-studied Li^+ migration mechanism, two control samples PVDF-HFP + LiFSI (PH) and PVDF-HFP + LiFSI + LLZTO (PH + LLZTO) were also prepared and compared. The details about the preparation method of these two control samples can be found in the experimental section.

To improve the performance of the electrolyte, the composition of PVDF-HFP, LLZTO, and LiFSI was systematically optimized. The mass ratio of PVDF-HFP/LiFSI with 1/1 in the PH system seems the best among all ratios in terms of ionic conductivity (Figure S2) and mechanical robustness (Figure S3). With the ratio increasing from 1/1 to 1/1.1, although ionic conductivity increases from 0.22 to 0.23, the mechanical property dramatically declines. As well known, the high salt concentrations may form undissociated ion pairs or ion clusters, although these clusters can provide a certain degree of physical crosslinking. At high concentrations, they tend to disrupt the continuity of the polymer chains, thereby reducing the ductility and strength of PVDF-HFP. As a result, PVDF-HFP/LiTFSI with a 1/1 ratio was used in the following study. To reveal the influence of LLZTO content on hybrid solid-state electrolyte, a series of samples were synthesized and compared. As presented in Figure S4, the PH + LLZTO system exhibits a volcano trend for ionic conductivity, and LLZTO with ~12 wt% shows the highest ionic conductivity of 0.66 mS cm^{-1}, which is the typical percolation threshold. To well illustrate the function of Li^+ bridges linking PVDF-HFP and LLZTO, LLZTO with 10 wt% was selected to prepare the PH-LLZTO system to compare with the other two systems to exclude the contribution from percolation behavior. These three solid-state electrolytes typically represent three types of ionic diffusion mechanisms (Figure 1B), and we try to understand the difference in Li^+ migration mechanisms among these three systems. The PH system shows that Li^+ migration relies solely on polymer chain relaxation, which is discontinuous and inefficient, probably resulting in relatively low electrochemical performance. With the introduction of LLZTO fillers into the PH system, a new Li^+ pathway is constructed apart from polymer chain relaxation, which will enhance Li^+ diffusion kinetics compared to the PH system. Increasing the LLZTO content to the percolation threshold, it can be found that a continuous Li^+ diffusion path is created along these ceramics, which will significantly boost Li^+ transport kinetics, as evidenced by Figure S4. However, these percolated ion-conduction pathways still leave room for further improvement, as they primarily rely on increasing filler content for construction, and the interfacial conduction remains relatively insufficiently stable. In the PH-LLZTO system, the interphase between PVDF-HFP and LLZTO is eliminated by constructing Li^+ bridges. Will these bridges further raise Li^+ transport kinetics in the bulk electrolyte? This is an interesting question.

Before answering the above question, whether those bridges successfully constructed between polymer and ceramics needs to be investigated. As shown in Figure S5B,C, the S 2p and O 1s peaks of LBS take an obvious shift after coating on LLZTO, indicating the strong coordination between LBS and LLZTO.[36] Meanwhile, the peaks at 1035 and 1127 cm^{-1} in Fourier transform infrared (FTIR) spectra assigned to S═O symmetric and asymmetric vibrations of LBS take a red shift after LLZTO interfacial coupling (Figure S6). In addition, the x-ray diffraction (XRD) pattern in Figure 2A also demonstrates the successful bonding between LLZTO and LBS, as evidenced by LLZTO-LBS patterns. These results well suggest that coordination interactions exclusively occur at the LLZTO surface without compromising its bulk crystallinity or phase integrity. Transmission electron microscope (TEM) analysis corroborates these findings, revealing that the LLZTO surface is conformally coated by a uniform, ~5 nm-thick LBS multilayer (Figure 2C). Such uniformity is enabled by a rigorous preparation protocol, in which the LBS solution is precisely dropped onto

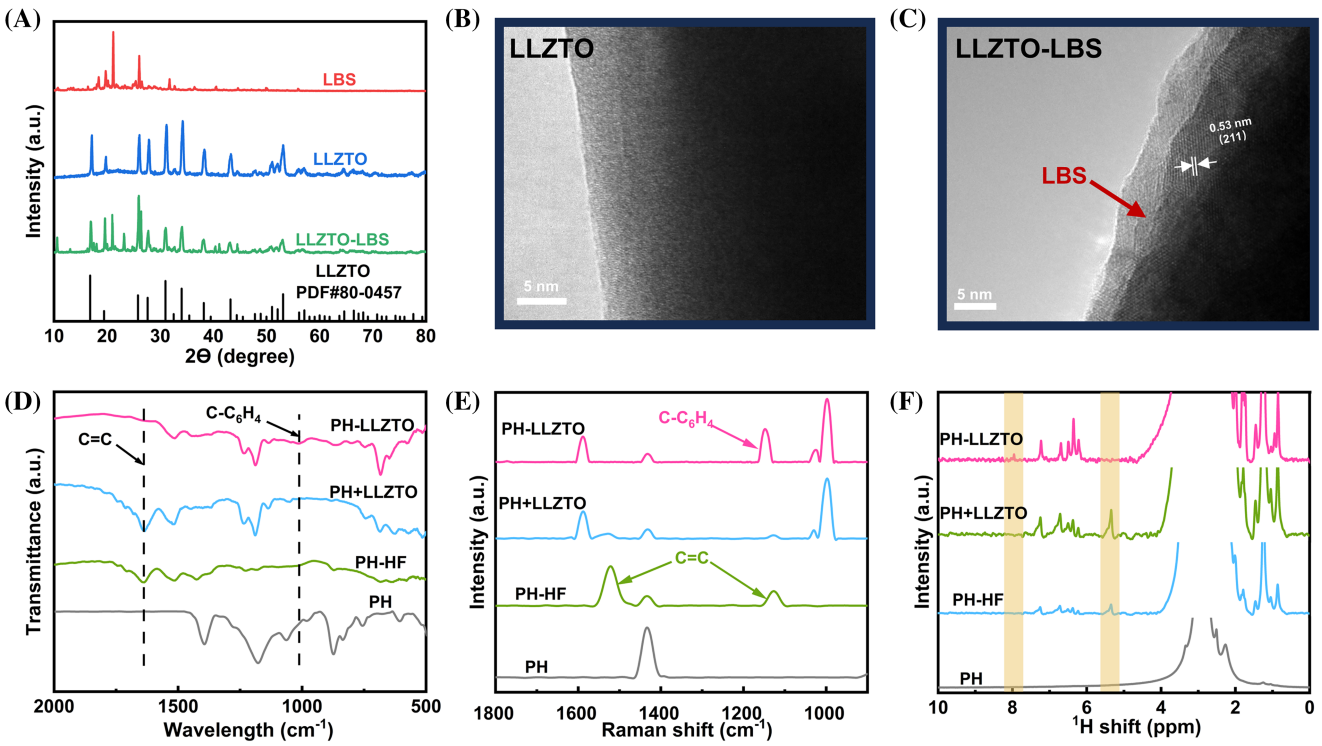

FIGURE 2 (A) XRD patterns of LBS, LLZTO, and LLZTO-LBS. (B) TEM image of LLZTO. (C) TEM image of LLZTO-LBS. (D) FTIR spectra of PH, PH-HF, PH + LLZTO, and PH-LLZTO polymer. (E) Raman spectra of PH, PH-HF, PH + LLZTO, and PH-LLZTO polymer. (F) ^{1}H NMR spectra of PH, PH-HF, PH + LLZTO, and PH-LLZTO polymer.

the LLZTO surface with a carefully controlled dripping rate and time to ensure reproducible coating thickness. Insufficient loading (incomplete coverage) or excessive loading (aggregation) results in non-uniform LBS layers, thereby leading to reduced ionic conductivities (Figure S7).

Depth-profiling XPS spectra (Figure S8) further confirm the uniform coating of LBS with a thickness of 5 nm, as evidenced by La 3d signals appearing after ~5 nm etching under testing two random spots. Importantly, the appearance of new S 2p signals after ~5 nm etching provides direct evidence that LBS is chemically anchored on LLZTO surfaces. All these results well suggest that LBS is successfully linked with LLZTO.

To further check whether these Li^+ bridges successfully link with PVDF-HFP, FTIR, Raman, and ^{1}H nuclear magnetic resonance (NMR) spectra were tested. To minimize the potential interference from FSI^- anions, LiFSI is intentionally excluded from the following spectra test. As disclosed in FTIR analysis (Figure 2D), a distinct vibrational signature at 1650 cm^{-1} appears in PH-HF compared to PH, which can be attributed to the formation of C═C stretching mode.[39] Besides, two characteristic peaks at 1520 and 1127 cm^{-1} in Raman spectra of PH-HF (Figure 2E)[40] and a peak at ~5.33 ppm in ^{1}H NMR spectra (Figure 2F) again verify C═C bonds in PH-HF. Upon successful completion of the LLZTO grafting reaction, the characteristic C═C stretching vibration peak completely disappears, while a distinct new vibrational peak at 1012 cm^{-1} appears in PH-LLZTO (Figure 2D),[34] corresponding to C—C_6H_4 stretching mode, providing direct spectral evidence of successful connection between LLZTO and PH-HF. Meanwhile, the peaks corresponding to polyenes of PH-LLZTO in Raman and ^{1}H NMR spectra disappear, but a new peak corresponding to the C—C_6H_4 stretching vibration appears at 1146 cm^{-1} (Figure 2E) and ~7.95 ppm (Figure 2F),[41] well matching with FTIR results. All these evidences demonstrate that the Li^+ bridges channels are successfully constructed, which may accelerate ionic transport kinetics in HSEs.

With the successful Li^+ bridges, PH-LLZTO is expected to present superior properties compared to PH and PH + LLZTO. As shown in Figure 3A, the as-prepared PH-LLZTO exhibits a relatively dense surface compared to PH and PH + LLZTO (Figure S10), which is contributed to by the interfacial bonding of LLZTO-PVDF-HFP, suggesting probably an efficient Li^+ pathway along this dense HSE.[42] The density and porosity of these three systems were characterized. As summarized in Table S1, the mass density of PH, PH + LLZTO, and PH-LLZTO are 1.21, 1.28, and 1.32 mg mm^{-3}, respectively, whereas the corresponding porosities of these three

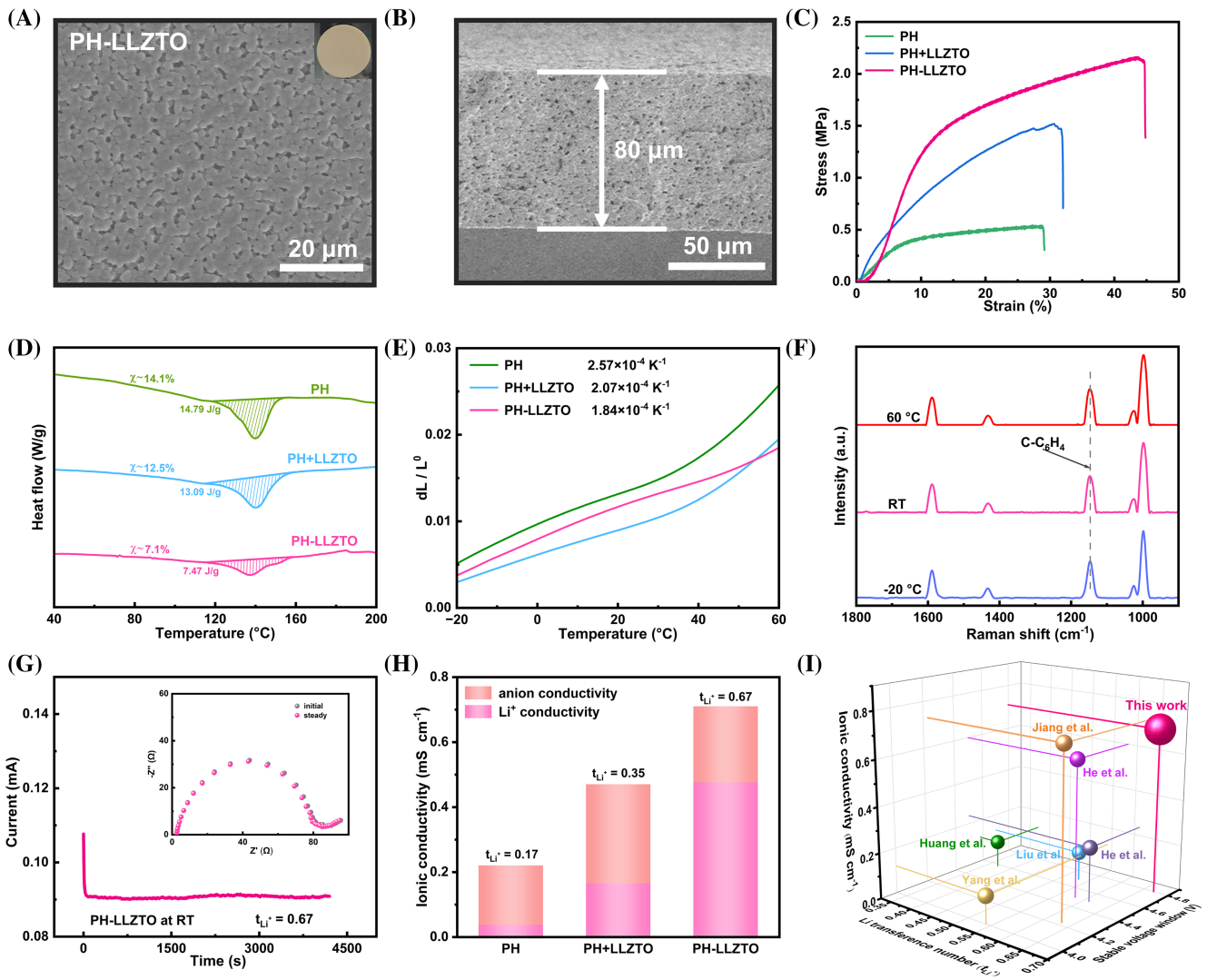

FIGURE 3 (A) Surface SEM image of PH-LLZTO electrolyte. The inset is the digital photo of PH-LLZTO. (B) Cross-sectional SEM image of PH-LLZTO electrolyte. (C) The stress–strain curves of PH, PH + LLZTO, and PH-LLZTO electrolytes. (D) DSC spectra of PH, PH + LLZTO, and PH-LLZTO electrolytes. (E) Thermal expansion coefficients of PH, PH + LLZTO, and PH-LLZTO in the range of −20°C to 60°C. (F) Raman spectra of PH-LLZTO polymers at different temperatures. (G) Li^+ transference number measurement of PH-LLZTO electrolyte. (H) Ionic conductivity and Li^+ transfer number of three electrolytes systems. (I) Comparing the electrical performance of recently reported work with this work. More information can be found in Table S1.

systems are 64.6%, 51.5%, and 46.7%, calculated by the mercury intrusion porosimetry method. These data are consistent with the conclusion from the SEM images. While such a dense structure may significantly enhance mechanical properties. As shown in Figure 3C, PH-LLZTO indeed presents the highest stress and strain among all samples, that is, 2.15 MPa and 44%, higher than those of PH + LLZTO (1.52 MPa, 32%) and PH (0.53 MPa, 28%). Will the superior mechanical property of PH-LLZTO affect its polymer crystallinity? As is well known, higher polymer crystallinity leads to poor ionic conductivity. With this question, differential scanning calorimetry (DSC) was conducted. As depicted in Figures 3D and S12, the crystallinity of PH-LLZTO remarkably decreases to 7.1% compared to PH (14.1%) and PH + LLZTO (12.5%). The calculation details can refer to the experimental section. Similarly, PH-LLZTO also presents the lowest glass-transition (T_g) of −58.61°C among PH (−45.4°C) and PH + LLZTO (−55.74°C). These results indicate that LLZTO fillers effectively disrupt the crystallinity of PVDF-HFP and enhance chain segmental flexibility, especially those connected to LBS. Surprisingly, PH-LLZTO with the lowest crystallinity presents the highest thermal stability among all samples, as suggested by the highest weight (94.3%) compared to PH + LLZTO (90.3%) and PH (87.1%) until the melting

temperature of 150°C, at which the polymer chains are fully extended (Figure S13).[43] This superior stability is attributed to interfacial bridges between LLZTO and PVDF-HFP, which effectively improve high-temperature resistance. In addition, the thermal expansion coefficients of PH with $2.57 \times 10^{-4}\ K^{-1}$, PH + LLZTO with $2.07 \times 10^{-4}\ K^{-1}$, and PH-LLZTO with $1.84 \times 10^{-4}\ K^{-1}$ again demonstrate the excellent thermal stability of the PH-LLZTO system (Figure 3E), which is contributed to by those Li^+ bridges. Beyond the macroscopic stability, the PH-LLZTO system also exhibits remarkable robustness against temperature variations at the molecular level. As evidenced by Raman spectra in Figure 3F, the characteristic vibration peak of the C—C_6H_4 segment remains clearly observable at −20°C, room temperature, and 60°C, confirming that the bridged ionic channels are stable across the entire temperature window. These results demonstrate well that the bridged ionic channels will not break up as caused by the thermal expansion or contraction of the polymer with temperature, which will effectively sustain continuous ion-conduction networks, thereby enabling a temperature-insensitive and robust Li^+ transport pathway. It can be expected that the as-designed Li^+ bridges between LLZTO and PVDF-HFP not only facilitate efficient ion transport but also endow the electrolyte with exceptional thermal endurance and mechanical resilience. Such a structural design imparts the HSE with relatively wide-temperature adaptability and outstanding interfacial stability, thereby positioning it as a highly promising platform for next-generation solid-state lithium metal batteries.

To further systematically investigate the influence of ionic bridge networks on PH-LLZTO electrolytes, a series of electrochemical characterizations has been systematically performed. The electrochemical working window is a critical parameter for pairing with high-voltage cathodes. As shown in Figure S14, the linear sweep voltammetry (LSV) curves reveal that PH-LLZTO exhibits the widest window of 4.8 V, compared to PH (4.4 V) and PH + LLZTO (4.5 V), which can be attributed to the suppression of PVDF-HFP decomposition by the interfacial bridges. Ionic conductivity serves as another pivotal functional determinant in HSEs. From Figure S15, it can be calculated that the PH-LLZTO electrolyte achieves superior ionic conductivity of 0.71 mS cm^{-1} at 25°C, which is 3.3 times higher than PH (0.22 mS cm^{-1}) and 1.5 times higher than PH + LLZTO (0.47 mS cm^{-1}). Based on the Arrhenius equation, the activation energy (E_a) of PH-LLZTO is calculated to be 0.19 eV, while the E_a of PH and PH + LLZTO electrolytes is 0.27 and 0.25 eV, respectively (Figure S16). A reduced activation energy indicates that Li^+ can migrate rapidly in bulk solid-state electrolyte,[44,45] which can be attributed to these as-constructed Li^+ bridges. The Li^+ transfer number (t_{Li}^+) describes the contribution of Li^+ conductivity to the overall ionic conductivity, and a higher t_{Li}^+ indicates fast Li^+ transport kinetics. Conventional SPEs typically exhibit a low t_{Li+} (<0.3) due to the Lewis base center of the polymer coupling with Li^+, resulting in slow migration mobility.[46] As depicted in Figures 3G and S17, the t_{Li+} of the PH-LLZTO electrolyte is calculated to be 0.67 based on the Vincent-Bruce equation, surpassing PH (0.17) and PH + LLZTO (0.36), which is intimately associated with the construction of Li^+ bridges. As shown in Figure S18, the ^{19}F resonance in PH-LLZTO exhibits a distinct downfield shift of 0.15 ppm compared with PH and PH + LLZTO, indicating that anions in PH-LLZTO are subjected to stronger immobilization.[47] This stronger immobilization originates from the synergistic effects of anion adsorption on the LLZTO surface together with additional confinement imposed by the bridged ionic network, which collectively suppress local dynamics and limit diffusional mobility. To evaluate the properties of this PH-LLZTO electrolyte thoroughly, previously reported PVDF-based electrolytes across three critical metrics, that is, ionic conductivity, t_{Li}^+, and stable voltage window, are compared and summarized in Figure 3I and Table S2. It is encouraging that our designed PH-LLZTO electrolyte exhibits the best electrochemical properties. Furthermore, as shown in Figure S19, to ensure the reliability of these results, ionic conductivity, Li^+ transference number, and electrochemical window test data are all presented with error bars (mean ± standard deviation), each derived from three independently prepared samples, and representative repeatability tests are shown in Figure S20.

With these superior electrochemical properties, the PH-LLZTO electrolyte is expected to show significant promise for implementation in LMBs systems. In Figures 4A and S21, Li|PH-LLZTO|Li symmetric cells can stably operate for more than 1150 h at 0.1 mA cm^{-2}. When the current density increases to 0.2 mA cm^{-2}, it can maintain stability till 1000 h with negligible voltage fluctuations, which is much longer than Li|PH + LLZTO|Li (around 276 h) and Li|PH|Li (around 142 h) cells. Moreover, Li|PH-LLZTO|Li symmetric cells exhibit stable cycling across 0.1–0.5 mA cm^{-2} with no short-circuiting. The overpotential is around 180 mV at 0.5 mA cm^{-2}, and it reduces to 40 mV upon reverting to 0.1 mA cm^{-2}, highlighting the excellent rate performance of Li|PH-LLZTO|Li cells. In contrast, when the current density reaches 0.3 mA cm^{-2}, the other symmetric batteries experience abrupt polarization fluctuations and short-circuiting (Figure 4B). A higher current density of 0.5 mA cm^{-2} was operated on Li|PH-LLZTO|Li cells to study the cycling performance. As shown in Figure 4C, it

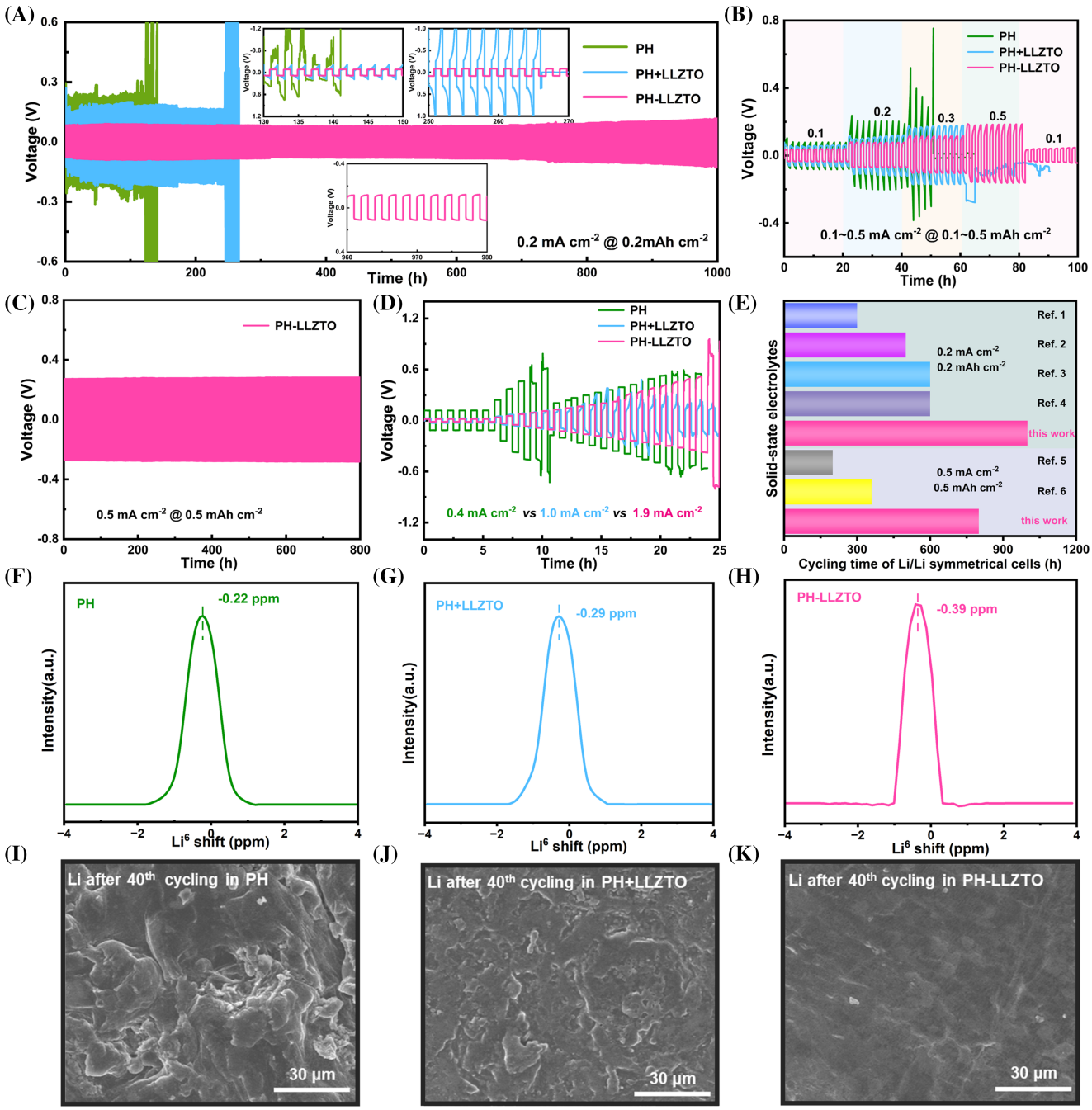

FIGURE 4 (A) Long-term cycling performance of Li/Li symmetric cells in three electrolyte systems at a current density of 0.2 mA cm^{-2} with a capacity of 0.2 mAh cm^{-2}. The insets are magnified voltage profiles of the various cycles. (B) Rate performance of symmetric Li/Li cells. (C) Voltage profiles of Li/Li symmetric cells in the PH-LLZTO electrolyte system at a current density of 0.5 mA cm^{-2} with a capacity of 0.5 mAh cm^{-2}. (D) Critical current density (CCD) of three electrolytes. (E) Comparison of Li/Li symmetric cells cycling time with recently reported work at 0.2 and 0.5 mA cm^{-2}. (F–H) ^{6}Li NMR spectra of PH, PH + LLZTO, and PH-LLZTO electrolytes. (I–K) Surface SEM images of cycled Li metal using different electrolyte systems.

achieves stable cycling up to 800 h, which is quite impressive among solid-state electrolyte systems. What's more, as depicted in Figure 4D, the Li|PH-LLZTO|Li symmetric batteries demonstrate a critical current density (CCD) of 1.9 mA cm^{-2}, much higher than PH + LLZTO (1.0 mA cm^{-2}) and PH (0.4 mA cm^{-2}), respectively. More importantly, the Li|PH-LLZTO|Li system demonstrates exceptional superiority over other reported Li/Li symmetrical cells utilizing PVDF-based SPEs at 0.2 and 0.5 mA cm^{-2} (Figure 4E and Table S3).

The ^{6}Li solid-state NMR further reveals the fundamental origin of the superior electrochemical

performance of PH-LLZTO. As seen in Figure 4F–H, the Li resonance shifts from −0.22 ppm in PH to −0.29 ppm in PH + LLZTO, indicating preferential coordination of Li^+ with O^{2-} from LLZTO and weakened Li^+-FSI^- interaction, accompanied by a narrower full width at half maximum (FWHM) suggesting faster Li^+ mobility. Remarkably, PH-LLZTO exhibits a further downfield shift to −0.39 ppm with an even narrower FWHM, which is attributed to the formation of Li^+ bridges (LBS). These bridges transform the interphase from physical adsorption (PH + LLZTO) to chemical bonding (PH-LLZTO), constructing a continuous, highly shielded conduction pathway that excludes FSI^- anions and enables significantly accelerated Li^+ dynamics.

Such accelerated Li^+ transport directly contributes to the stable Li deposition behavior. The cycled-Li anode morphology was studied by SEM. As shown in Figure 4I–K, the bumpy Li surface can be observed after 40 cycles in PH and PH + LLZTO systems; whereas the PH-LLZTO system exhibits a relatively uniform Li deposition morphology, indicating that PH-LLZTO facilitates a stable Li plating/stripping process. To unveil whether surface chemistry affects the above symmetric cell performance, XPS was used to analyze the solid electrolyte interphase (SEI) composition on cycled Li metal anodes based on the different electrolyte systems. As shown in Figures S22 and S23, PH and PH + LLZTO systems derive an organic-rich SEI compared to PH-LLZTO. The organic-rich SEI is regarded as a poor Li^+ conductor, which slows down Li^+ migration along the SEI and exhibits inferior mechanical property.[48,49] Based on these two features, the PH and PH + LLZTO systems with organic-rich SEI behave not as well as PH-LLZTO. These abundant organic components derived in the PH and PH + LLZTO systems originate from residual solvent decomposition and polymer decomposition.[50] By contrast, PH-LLZTO effectively suppresses the generation of organic species through two synergistic effects: ceramic fillers immobilize residual solvents, thereby suppressing their interfacial decomposition,[25] and enhancing polymer robustness to inhibit decomposition and defluorination,[51] ultimately resulting in an inorganic-rich SEI that stabilizes Li/Li cycling.

With the excellent features of this PH-LLZTO solid-state electrolyte, it is expected to assist batteries with superior performance. Herein, a high-voltage $LiNi_{0.8}Co_{0.1}Mn_{0.1}O_2$ (NCM811) cathode was used to evaluate the potential of this PH-LLZTO electrolyte. The Nyquist plots of three systems were tested and shown in Figure 5A. According to the equivalent circuit, the impedance spectra can be interpreted as the series connection of R_b (bulk resistance of the solid electrolyte), R_{int} (interfacial impedance) and W (Warburg impedance) (Figure S24). R_{int} can be modeled by a parallel combination of the charge transfer resistance (R_{ct}) and a double-layer capacitor (Q1). From Figure S25 and Table S4, it can be found that the PH-LLZTO system exhibits the smallest R_b compared to the other two systems, suggesting the highest bulk ionic conductivity, which is contributed by the dramatic improvement in the interfacial compatibility between the hydrophilic LLZTO ceramic and the hydrophobic PVDF-HFP polymer matrix through Li^+ bridges. These Li^+ bridges create continuous and low-resistance ion transport networks, thus significantly enhancing Li^+ diffusion kinetics. Similarly, the PH-LLZTO system presents the smallest R_{ct}, which well demonstrates that a stable and high-Li^+-conductive electrode/electrolyte interphase in the PH-LLZTO system presents a lower energy barrier for Li^+ migration and charge transfer compared to the PH and PH + LLZTO systems. It is noteworthy that Warburg diffusion becomes the dominant feature in the PH-LLZTO system compared to the other two systems, well reflecting the superior bulk and interfacial resistances in PH-LLZTO. In Figure S26, the σ_w (Warburg factor) of PH, PH + LLZTO and PH-LLZTO are 1081.7, 934.2 and 248.9, respectively, indicating that these Li^+ bridges significantly reduce the diffusion resistance and enable faster Li^+ transport. Benefiting from the above advantages, the NCM811|PH-LLZTO|Li batteries exhibit highly stable cycling performance at 0.5 C under ambient conditions (25°C). As shown in Figures 5B and S27, the initial discharge capacity of the NCM811|PH-LLZTO|Li cell is 165 mAh g^{-1}. Even after 300 cycles, the capacity retention remains almost 80%. On the contrary, the initial discharge capacity of the PH electrolyte is only 153 mAh g^{-1} and an obvious short circuit appears after 60 cycles. The NCM811|PH + LLZTO|Li cell achieves a discharge capacity of 160 mAh g^{-1}; however, the capacity retention is only 12.5% of the initial discharge capacity after 300 cycles (20 mAh g^{-1}). To further verify practical applicability, electrochemical tests were conducted on NCM811|PH-LLZTO|Li cells with a high cathode loading of 5 mg cm^{-2} (Figure S28). It still delivers stable cycling performance with an initial specific capacity of 165 mAh g^{-1} over 30 cycles, along with a coulombic efficiency consistently above 99.2%. In addition, as demonstrated in Figures 5C and S29, NCM811|PH-LLZTO|Li delivers a discharge capacity of 175, 161, 152, 143, and 129 mAh g^{-1} at 0.1, 0.5, 1, 2, and 4 C, respectively; it can return to 158 mAh g^{-1} when the current density returns to 0.5 C, much higher than the PH and PH + LLZTO systems. Although the initial discharge capacity of the PH + LLZTO electrolyte at 0.1 C is the same as the PH-LLZTO system, the capacity decreases significantly when it reverts to 0.5 C after completing a high current density

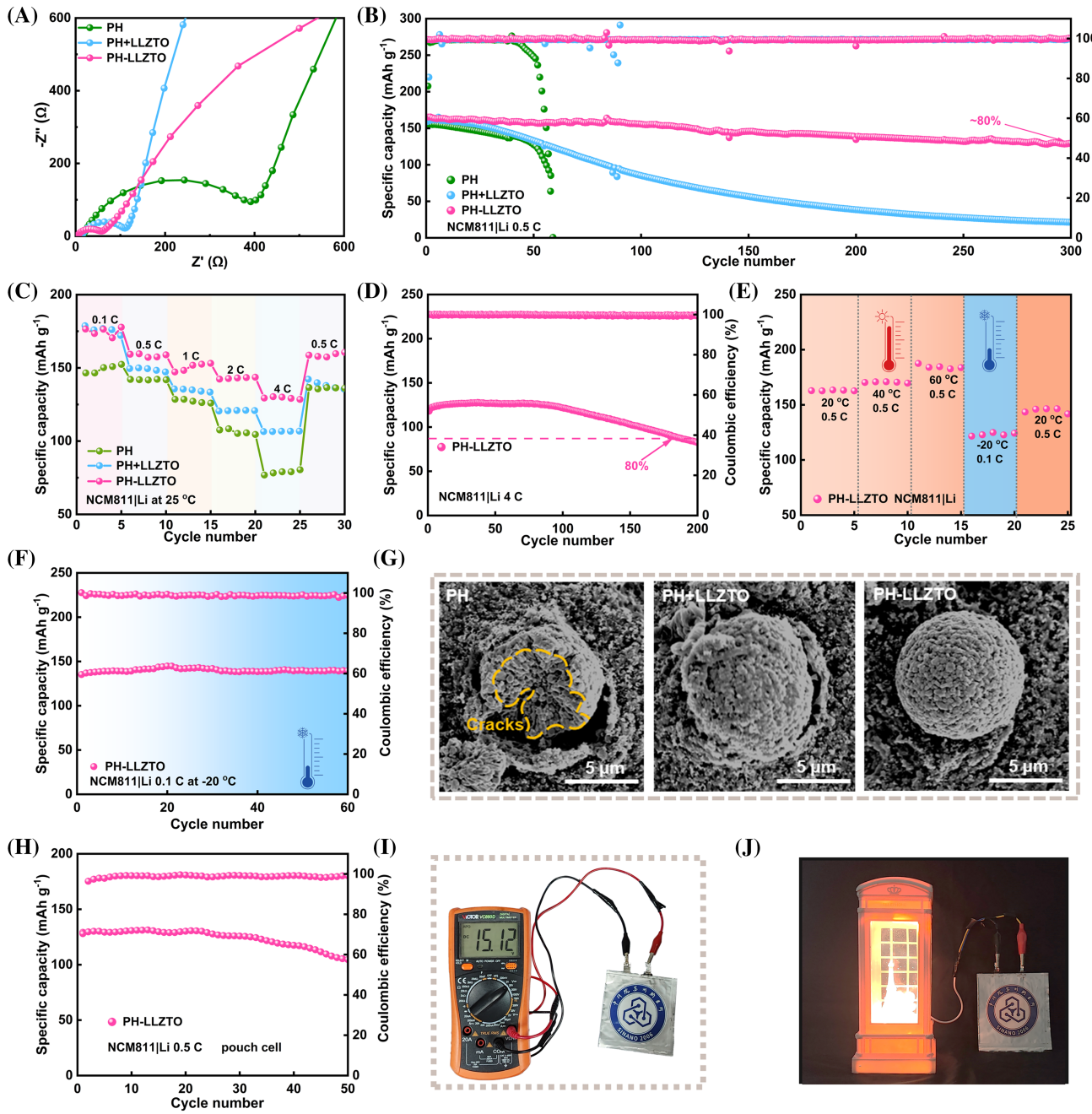

FIGURE 5 (A) Nyquist plots of NCM811/Li system with PH, PH + LLZTO, and PH-LLZTO electrolytes. (B) Cycling performance of NCM811/Li cells with the PH, PH + LLZTO, and PH-LLZTO electrolytes at 0.5 C under 25°C. (C) Rate performance of NCM811/Li batteries using three electrolytes. (D) Cycle stability of NCM811/Li cells with PH-LLZTO electrolyte at 4 C. (E) Cycling performance of NCM811/Li batteries with PH-LLZTO electrolyte under a wide temperature range from −20°C to 60°C. (F) Electrochemical performance of NCM811/Li batteries with PH-LLZTO electrolyte at −20°C. (G) Top-view SEM morphologies of NCM811 cathode subjected to 50 cycles using PH, PH + LLZTO, and PH-LLZTO. (H) The cycling performance of NCM811/Li pouch cell with PH-LLZTO at 0.5 C. (I) Bipolar pouch cell with a high-output voltage of 15.12 V. (J) Optical photographs of the bipolar pouch cell lighting up a 5 V music box.

cycle at 4 C, which is due to the sluggish Li^+ migration speed when crossing the interphase between LLZTO and PVDF-HFP. These results again demonstrate the efficiency of Li^+ bridges in tackling the classic issue in the mixed polymer and ceramic solid-state electrolyte systems. Figure 3F well presents the robustness of these Li^+ bridges across a wide temperature range. To further push this excellent PH-LLZTO system, comprehensive electrochemical tests were implemented under harsh conditions, including high-rate cycling, high-voltage conditions and a wide temperature range. The cycling performance test with PH-LLZTO electrolyte at a high current density of 4 C is shown in

Figure 5D. The discharge capacity gradually increased from 120 mAh g^{-1} to around 128 mAh g^{-1} during initial cycling, followed by stable retention of 80% capacity over 170 cycles, indicating the superior Li^+ transport kinetics of PH-LLZTO. Under a wide temperature range of −20 to 60°C, NCM811|PH-LLZTO|Li cells also display well. As shown in Figure 5E, they deliver a discharge capacity of 163 mAh g^{-1} at 20°C, 170 mAh g^{-1} at 40°C, 184 mAh g^{-1} at 60°C, and 122 mAh g^{-1} at −20°C, respectively; and they return to 146 mAh g^{-1} at 20°C after experiencing 5 cycles at such a low temperature, −20°C. Besides, PH-LLZTO supports cells working under low temperatures and high temperatures for certain cycles. At −20°C, NCM811/Li cells deliver a discharge capacity of around 130 mAh g^{-1} and can stably cycle for more than 60 times without any capacity decay with Coulombic efficiency (CE) above 99% (Figures 5F and S31). At 60°C, NCM811/Li cells present an initial discharge capacity of ∼170 mAh g^{-1} with nearly 99% retention after 60 cycles (Figure S32) at 1 C, obviously surpassing PH (40% retention) and PH + LLZTO (88% retention). To evaluate this PH-LLZTO well, its performance in NCM811/Li cells (including capacity retention, cycle number, current rate, mass loading and minimum temperature) is summarized and compared with recently reported PVDF-based solid-state electrolytes. As seen in Figure S33 and Table S5, the PH-LLZTO electrolyte exhibits outstanding overall performance across all these critical criteria.

To further inspect the contributions for these impressive behaviors, the cathode/electrolyte interphase was carefully investigated. As shown in Figure 5G, some cracks can be clearly observed in cycled NCM811 particles in PH and PH + LLZTO systems, while cycled NCM811 particles in PH-LLZTO seem relatively smooth and intact, reflecting the stable interphase of PH-LLZTO and the cathode. Those as-constructed Li^+ bridges reinforce the mechanical property of polymer chains, thus suppressing decomposition or side reactions under high voltage. Thus, it can be found that the PH-LLZTO system presents a thin and uniform CEI with 10 nm thickness; however, the PH + LLZTO system derives a thick CEI with 14 nm thickness and the PH system forms a CEI with 22 nm thickness (Figure S34A–C). As well known, a thicker CEI results in larger resistance, especially under harsh conditions, such as low temperature, high voltage, etc. XPS tests on the CEI demonstrate that an inorganic-rich CEI is formed in the PH-LLZTO system, which is similar to SEI (Figure S34D). Compared to an organic-rich CEI, the inorganic component shows higher hardness, which can protect NCM particles during cycling to some extent. In all, a thin CEI with an inorganic-rich component enhances interphase stability along cycling, thereby empowering high performance under harsh conditions. Consequently, as seen in Figure 5H, the NCM811/Li pouch cell with PH-LLZTO electrolyte reaches up to 50 cycles with an initial discharge capacity of around 130 mAh g^{-1} at 0.5 C, while maintaining functionality to power a light-emitting diode (LED) during bending, folding, and even partial cutting (Figure S35). Moreover, as shown in Figure S36, when the cathode mass loading increased to approximately 18.3 mg cm^{-2}, the pouch cell delivers a discharge capacity of 44.8 mAh and a gravimetric energy density of 311.9 Wh kg^{-1} can be achieved (Table S6). From Video S1 with 16× accelerated speed, it can be found that the NCM811|PH-LLZTO|Li pouch cell works functionally at −20°C for lighting an LED for over 90 min (Supporting Information), demonstrating the potential application of this PH-LLZTO-assisted solid-state batteries under low temperature. Besides, based on our previous experience with assembling bipolar structure,[52,53] a bipolar pouch cell was successfully constructed by stacking 4 units with an ultra-high voltage output of 15.12 V (Figure 5I). It powers a 5 V lamp (Figure 5J and Video S2), showcasing the great potential of integrated module application in the future.

3 | CONCLUSIONS

In summary, a novel high-performance solid-state electrolyte has been achieved by bridging LLZTO ceramic with PVDF-HFP segment, resolving interfacial impedance in HSEs to enable high-performance LMBs. With these Li^+ bridges, PH-LLZTO exhibits high ionic conductivity (0.71 mS cm^{-1} at 25°C), which enables Li|PH-LLZTO|Li cycling for 1000 h at 0.2 mA cm^{-1}, and 800 h at 0.5 mA cm^{-1}. Furthermore, the solid-state NCM811|PH-LLZTO|Li batteries could stably work for 300 cycles with a capacity retention around 80% at 0.5 C. Meanwhile, this solid-state battery withstands extreme operational challenges, that is, high-rate cycling (4 C) and wide temperature range (−20°C to 60°C), and the pouch cell works functionally under a commercial-grade areal capacity (3.44 mAh cm^{-2}). This work proposes an engineered highly efficient, single-ion-conductor-like interfacial transport (chemically integrated ionic network), instead of ceramic-percolation enhanced interfacial transport (physical mixture) for efficiently enhancing Li^+ transport kinetics, which represents a new paradigm to design advanced solid-state electrolyte in the future.

4 | EXPERIMENTAL SECTION

4.1 | Preparation of LBS and LLZTO-LBS

Lithiumbenzene sulfonate (LBS) was synthesized by mixing benzene sulfonic acid (BS, Aladdin) with lithium hydroxide (LiOH, Aladdin) under continuous stirring

with a molar ratio of 1:1. Then evenly apply the LBS solution onto the surface of $Li_{6.4}La_3Zr_{1.4}Ta_{0.6}O_{12}$ (LLZTO) through careful control of the dripping rate and time and vacuum drying at 80°C to remove solvent.

4.2 | Preparation of PH-LLZTO electrolyte

The composite solid electrolytes (CSEs) were prepared by a simple solution-casting method. Poly(vinylidene fluoride-co-hexafluoropropylene) (PVDF-HFP) ($Mn = 1.1 \times 10^{-5}$, Sigma-Aldrich) and LiOH were dissolved in N, N-dimethylformamide (DMF) solvent at a monomer molar ratio of 10:1 under magnetic stirring for more than 24 h at 60°C to obtain dehydrofluorinated PVDF-HFP solution (PH-HF). Then, LLZTO-LBS was added to the PH-HF solution with a small amount of $AlCl_3$ (Aladdin, 99%) and stirring continued at 60°C for more than 12 h. In addition, the solution without adding $AlCl_3$ is recorded as PH + LLZTO. Finally, Lithium bis(fluorosulfonyl)imide (LiFSI) (99.9%, Duoduo Chem Co., Ltd.) was added and stirred for 12 h to obtain PH-LLZTO solution. After that, the as-obtained solution was cast on a clean glass substrate by the solution-casting method to obtain PH-LLZTO composite polymer electrolyte membrane via a heating treatment at 60°C in a vacuum oven for 24 h. The mass ratio of PVDF-HFP to LiFSI is 1:1, and the weight ratio of LLZTO-LBS is 10 wt% of the total mass of PVDF-HFP, LiFSI, and LLZTO-LBS.

AUTHOR CONTRIBUTIONS

Yuchen Wang: Conceptualization; methodology; investigation; writing—original draft. **Kun Liu**: Formal analysis. **Henghui Xiao**: Methodology. **Zhaorun Zhu**: Methodology. **Chenqun Hong**: Methodology. **Hongzhen Lin**: Discussion. **Jian Wang**: Formal analysis; review and editing. **Decai Guo**: Characterization. **Meinan Liu**: Conceptualization; methodology; investigation; supervision; writing—review and editing.

ACKNOWLEDGMENTS

The financial support from the National Natural Science Foundation of China (22379160 and 22075313), Special Fund for Science and Technology Development of Guangxi (Grant No. AD25069078), and Open Project of State Key Laboratory of Inorganic Synthesis and Preparative Chemistry (2025-8) as well as the Opening funding from Key Laboratory of Engineering Dielectrics and Its Application (Harbin University of Science and Technology) (No. KFM202507, Ministry of Education) are acknowledged. The x-ray photoelectron spectroscopy (XPS) characterizations were supported by Nano-X, Suzhou Institute of Nano-Tech and Nano-Bionics (SINANO), Chinese Academy of Sciences. Dr. Jian Wang thanks the fellowship supported by the Alexander von Humboldt Foundation Fellowship. Open Access funding enabled and organized by Projekt DEAL.

CONFLICT OF INTEREST STATEMENT

The authors declare no conflicts of interest.

DATA AVAILABILITY STATEMENT

The data that support the findings of this study are available from the corresponding author upon reasonable request.

ORCID

Jian Wang https://orcid.org/0000-0002-7945-0826

REFERENCES

1. Li L, Wang M, Wang J, et al. Asymmetric gel polymer electrolyte with high lithium ion conductivity for dendrite-free lithium metal batteries. *J Mater Chem A*. 2020;8(16):8033-8040.
2. Tu H, Li L, Hu Y, et al. Non-flammable liquid polymer-in-salt electrolyte enabling secure and dendrite-free lithium metal battery. *Chem Eng J*. 2022;434(15):134647.
3. Goodenough JB, Park KS. The Li-ion rechargeable battery: a perspective. *J Am Chem Soc*. 2013;135(4):1167-1176.
4. Lin D, Liu Y, Cui Y. Reviving the lithium metal anode for high-energy batteries. *Nat Nanotechnol*. 2017;12(3):194-206.
5. Li L, Tu H, Wang J, et al. Electrocatalytic MOF-carbon bridged network accelerates Li^+-solvents desolvation for high Li^+ diffusion toward rapid sulfur redox kinetics. *Adv Funct Mater*. 2023;33(13):2212499.
6. Tu H, He Z, Sun A, et al. Superior Li^+ kinetics by "low-activity-solvent" engineering for stable lithium metal batteries. *Nano Lett*. 2024;24(19):5714-5721.
7. Sun A, Tu H, Sun Z, et al. Dual-halide interphase enabling high-performance lithium metal batteries in wide-temperature range. *ACS Energy Lett*. 2024;9(6):2545-2553.
8. Tu H, Li L, Wang Z, et al. Tailoring electrolyte solvation for LiF-rich solid electrolyte interphase toward a stable Li anode. *ACS Nano*. 2022;16(10):16898-16908.
9. Tarascon JM, Armand M. Issues and challenges facing rechargeable lithium batteries. *Nature*. 2001;414(6861):359-367.
10. Li M, Lu J, Chen Z, Amine K. 30 years of lithium-ion batteries. *Adv Mater*. 2018;30(33):1800561.
11. Hu Y, Li L, Tu H, et al. Janus electrolyte with modified Li^+ solvation for high-performance solid-state lithium batteries. *Adv Funct Mater*. 2022;32(32):2203336.
12. Xue Z, He D, Xie X. Poly (ethylene oxide)-based electrolytes for lithium-ion batteries. *J Mater Chem A*. 2015;3(38):19218-19253.
13. Chen WP, Duan H, Shi JL, et al. Bridging interparticle Li^+ conduction in a soft ceramic oxide electrolyte. *J Am Chem Soc*. 2021;143(15):5717-5726.
14. Zhang X, Wang S, Xue C, et al. Self-suppression of lithium dendrite in all-solid-state lithium metal batteries with poly (vinylidene difluoride)-based solid electrolytes. *Adv Mater*. 2019;31(11):1806082.

15. Wei Y, Liu TH, Zhou W, et al. Enabling all-solid-state Li metal batteries operated at 30°C by molecular regulation of polymer electrolyte. *Adv Energy Mater*. 2023;13(10):2203547.
16. Wu L, Wang Y, Tang M, et al. Lithium-ion transport enhancement with bridged ceramic-polymer interface. *Energy Storage Mater*. 2023;58:40-47.
17. Xiong BQ, Zhang J, Nian Q, et al. Long-life all-solid-state batteries enabled by cold-pressed garnet composite electrolytes with enhanced Li^+ conduction. *Angew Chem*. 2024;137(1): e202413502.
18. Lu Z, Peng L, Rong Y, et al. Enhanced electrochemical properties and optimized Li^+ transmission pathways of PEO/-LLZTO-based composite electrolytes modified by supramolecular combination. *Energy Environ Mater*. 2024;7(1):e12498.
19. Zha W, Li W, Ruan Y, Wang J, Wen Z. In situ fabricated ceramic/polymer hybrid electrolyte with vertically aligned structure for solid-state lithium batteries. *Energy Storage Mater*. 2021;36:171-178.
20. Zhao Z, Zhou X, Zhang B, et al. Regulating steric hindrance of porous organic polymers in composite solid-state electrolytes to induce the formation of LiF-rich SEI in Li-ion batteries. *Angew Chem Int Ed Engl*. 2023;62(39):e202308738.
21. Lu G, Liu W, Yang Z, et al. Superlithiophilic, ultrastable, and ionic-conductive interface enabled long lifespan all-solid-state lithium-metal batteries under high mass loading. *Adv Funct Mater*. 2023;33(49):2304407.
22. Li Z, Tang D, Wang W, et al. Construction of composite lithium with high adhesion work and fast ionic conductivity by black phosphorus for solid-state lithium batteries. *Nano Energy*. 2024;132:110356.
23. Li C, Mu Y, Deng T, et al. In situ construction of a 3D superionic skeleton in sodium anode for solid-state sodium batteries with a 15 000-cycle lifespan at 3C. *Adv Mater*. 2025; 37(20):2419190.
24. Lu G, Li M, Chen P, et al. Built-in superionic conductive phases enabling dendrite-free, long lifespan and high specific capacity composite lithium for stable solid-state lithium batteries. *Energ Environ Sci*. 2023;16(3):1049-1061.
25. Yang K, Chen L, Ma J, et al. Stable interface chemistry and multiple ion transport of composite electrolyte contribute to ultra-long cycling solid-state $LiNi_{0.8}Co_{0.1}Mn_{0.1}O_2$/lithium metal batteries. *Angew Chem Int Ed Engl*. 2021;60(46):24668-24675.
26. Wang N, Jia M, Bi Z, Guo X. Composite electrolytes with Li_2CO_3-free garnets achieved by one-step poly (propylene carbonate) treatment for high-rate and long-life solid lithium batteries. *Adv Funct Mater*. 2024;34(36):2401400.
27. Miao X, Guan S, Ma C, Li L, Nan CW. Role of interfaces in solid-state batteries. *Adv Mater*. 2023;35(50):2206402.
28. Liu M, Zhang S, van Eck ERH, Wang C, Ganapathy S, Wagemaker M. Improving Li-ion interfacial transport in hybrid solid electrolytes. *Nat Nanotechnol*. 2022;17(9):959-967.
29. Sand SC, Rupp JLM, Yildiz B. A critical review on Li-ion transport, chemistry and structure of ceramic-polymer composite electrolytes for solid state batteries. *Chem Soc Rev*. 2025;54(1): 178-200.
30. Fan LZ, He H, Nan CW. Tailoring inorganic-polymer composites for the mass production of solid-state batteries. *Nat Rev Mater*. 2021;6(11):1003-1019.
31. Shi P, Ma J, Liu M, et al. A dielectric electrolyte composite with high lithium-ion conductivity for high-voltage solid-state lithium metal batteries. *Nat Nanotechnol*. 2023;18(6): 602-610.
32. Zhu L, Chen J, Wang Y, et al. Tunneling interpenetrative lithium ion conduction channels in polymer-in-ceramic composite solid electrolytes. *J Am Chem Soc*. 2024;146(10):6591-6603.
33. Liu Y, Wang P, Yang Z, et al. Lignin derived ultrathin all-solid polymer electrolytes with 3D single-ion nanofiber ionic bridge framework for high performance lithium batteries. *Adv Mater*. 2024;36(27):2400970.
34. Mi J, Ma J, Chen L, et al. Topology crafting of polyvinylidene difluoride electrolyte creates ultra-long cycling high-voltage lithium metal solid-state batteries. *Energy Storage Mater*. 2022; 48:375-383.
35. Huang L, Fu H, Duan J, et al. Negating Li^+ transfer barrier at solid-liquid electrolyte interface in hybrid batteries. *Chem*. 2022;8(7):1928-1943.
36. Yang G, Bai X, Zhang Y, et al. A bridge between ceramics electrolyte and interface layer to fast Li^+ transfer for low interface impedance solid-state batteries. *Adv Funct Mater*. 2023;33(3): 2211387.
37. Brewis DM, Mathieson I, Sutherland I, Cayless RA, Dahm RH. Pretreatment of poly (vinyl fluoride) and poly (vinylidene fluoride) with potassium hydroxide. *Int J Adhes Adhes*. 1996;16(2): 87-95.
38. Hwang YY, Lee NK, Park SH, Shin J, Lee YJ. TFSI anion grafted polymer as an ion-conducting protective layer on magnesium metal for rechargeable magnesium batteries. *Energy Storage Mater*. 2022;51:108-121.
39. Li B, Su Q, Yu L, et al. $Li_{0.35}La_{0.55}TiO_3$ nanofibers enhanced poly(vinylidene fluoride)-based composite polymer electrolytes for all-solid-state batteries. *ACS Appl Mater Interfaces*. 2019; 11(45):42206-42213.
40. Zhang X, Liu T, Zhang S, et al. Synergistic coupling between $Li_{6.75}La_3Zr_{1.75}Ta_{0.25}O_{12}$ and poly(vinylidene fluoride) induces high ionic conductivity, mechanical strength, and thermal stability of solid composite electrolytes. *J Am Chem Soc*. 2017; 139(39):13779-13785.
41. Naseer K, Amin A, Saleem M, Qazi J. Raman spectroscopy based differentiation of typhoid and dengue fever in infected human sera. *Spectrochim Acta A Mol Biomol Spectrosc*. 2019; 206(5):197-201.
42. Wu Q, Fang M, Jiao S, et al. Phase regulation enabling dense polymer-based composite electrolytes for solid-state lithium metal batteries. *Nat Commun*. 2023;14(1):6296.
43. Liu W, Wang A, Yang R, et al. Water-triggered stiffening of shape-memory polyurethanes composed of hard backbone dangling PEG soft segments. *Adv Mater*. 2022;34(46): 2201914.
44. Wu N, Chien PH, Li Y, et al. Fast Li^+ conduction mechanism and interfacial chemistry of a NASICON/polymer composite electrolyte. *J Am Chem Soc*. 2020;142(5):2497-2505.
45. Wu N, Chien PH, Qian Y, et al. Enhanced surface interactions enable fast Li^+ conduction in oxide/polymer composite electrolyte. *Angew Chem Int Ed Engl*. 2020;59(10):4131-4137.
46. Zhai Y, Hou W, Tao M, et al. Enabling high-voltage "superconcentrated ionogel-in-ceramic" hybrid electrolyte with ultrahigh

ionic conductivity and single Li^+-ion transference number. *Adv Mater*. 2022;34(39):2205560.
47. Qiao B, Leverick GM, Zhao W, Flood AH, Johnson JA, Shao-Horn Y. Supramolecular regulation of anions enhances conductivity and transference number of lithium in liquid electrolytes. *J Am Chem Soc*. 2018;140(35):10932-10936.
48. Yang W, Liu Y, Sun X, He Z, He P, Zhou H. Solvation-tailored PVDF-based solid-state electrolyte for high-voltage lithium metal batteries. *Angew Chem*. 2024;136(18): e202401428.
49. Yang K, Ma J, Li Y, et al. Weak-interaction environment in a composite electrolyte enabling ultralong-cycling high-voltage solid-state lithium batteries. *J Am Chem Soc*. 2024;146(16): 11371-11381.
50. Zhang X, Han J, Niu X, et al. High cycling stability for solid-state Li metal batteries via regulating solvation effect in poly (vinylidene fluoride)-based electrolytes. *Batteries Supercaps*. 2020;3(9):876-888.
51. Castillo J, Robles-Fernandez A, Cid R, et al. Dehydrofluorination process of poly (vinylidene difluoride) PVdF-based gel polymer electrolytes and its effect on lithium-sulfur batteries. *Gels*. 2023;9(4):336.
52. Wang Y, Tu H, Sun A, et al. Dual Li^+ transport enabled by BN-assisted solid-polymer-electrolyte for high-performance lithium batteries. *Chem Eng J*. 2023;475(1):146414.
53. Wang L, Yi S, Liu Q, et al. Bifunctional lithium-montmorillonite enabling solid electrolyte with superhigh ionic conductivity for high-performanced lithium metal batteries. *Energy Storage Mater*. 2023;63:102961.

SUPPORTING INFORMATION

Additional supporting information can be found online in the Supporting Information section at the end of this article.

How to cite this article: Wang Y, Liu K, Xiao H, et al. Delicate design of lithium-ion bridges in hybrid solid electrolyte for wide-temperature adaptive solid-state lithium metal batteries. *InfoMat*. 2025;e70095. doi:10.1002/inf2.70095